Single-shot two-dimensional full-range optical coherence tomography achieved by dispersion control

Witte, S.; Baclayon, M.; Peterman, E.J.G.; Toonen, R.F.G.; Mansvelder, H.D.; Groot, M.L.

published in
Optics Express
2009

DOI (link to publisher)
10.1364/OE.17.011335

document version
Publisher's PDF, also known as Version of record

Single-shot two-dimensional full-range optical coherence tomography achieved by dispersion control

S. Witte[1,4], M. Baclayon[1,4], E. J. G. Peterman[1,4], R. F. G. Toonen[2,4], H. D. Mansvelder[3,4], and M. L. Groot[1,4]

[1]*Department of Physics and Astronomy, Faculty of Sciences, VU University*
[2]*Department of Functional Genomics, Centre for Neurogenomics and Cognitive Research, VU University*
[3]*Department of Integrative Neurophysiology, Centre for Neurogenomics and Cognitive Research, VU University*
[4]*Neuroscience Campus Amsterdam, VU University, De Boelelaan 1081, 1081 HV Amsterdam, The Netherlands*
switte@few.vu.nl

Abstract: We present a full-range Fourier-domain optical coherence tomography (OCT) system that is capable of acquiring two-dimensional images of living tissue in a single shot. By using line illumination of the sample in combination with a two-dimensional imaging spectrometer, 1040 depth scans are performed simultaneously on a sub-millisecond timescale. Furthermore, we demonstrate an easy and flexible real-time single-shot technique for full-range (complex-conjugate cancelled) OCT imaging that is compatible with both two-dimensional as well as ultrahigh-resolution OCT. By implementing a dispersion imbalance between reference and sample arms of the interferometer, we eliminate the complex-conjugate signal through numerical dispersion compensation, effectively increasing the useful depth range by a factor of two. The system allows us to record 6.7×3.2 mm images at 5 μm depth resolution in 0.2 ms. Data postprocessing requires only 4 s. We demonstrate the capability of our system by imaging the anterior chamber of a mouse eye *in vitro*, as well as human skin *in vivo*.

OCIS codes: (110.0110) Imaging systems; (170.4500) Optical coherence tomography; (320.1590) Chirping; (110.3010) Image reconstruction techniques; (070.0070) Fourier optics and signal processing; (100.5070) Phase retrieval

References and links

1. D. Huang, E.A. Swanson, C.P. Lin, J.S. Schuman, W.G. Stinson, W. Chang, M.R. Hee, T. Flotte, K. Gregory, C.A. Puliafito, and J.G. Fujimoto, "Optical coherence tomography," Science **254**, 1178–1181 (1991).
2. C.A. Puliafito, M.R. Hee, C.P. Lin, E. Reichel, J.S. Schuman, J.S. Duker, J.A. Izatt, E.A. Swanson, and J.G. Fujimoto, "Imaging of macular diseases with optical coherence tomography," Ophthalmology **102**, 217–229 (1995).
3. W. Drexler, U. Morgner, R.K. Ghanta, F.X. Kärtner, J.S. Schuman, and J.G. Fujimoto, "Ultrahigh-resolution ophthalmic optical coherence tomography," Nat. Med. **7**, 502–507 (2001).
4. N.A. Nassif, B. Cense, B.H. Park, M.C. Pierce, S.H. Yun, B.E. Bouma, G.J. Tearney, T.C. Chen, and J.F. de Boer, "In vivo high-resolution video-rate spectral-domain optical coherence tomography of the human retina and optic nerve," Opt. Express **12**, 367–376 (2004).
5. S. Asrani, M.V. Sarunic, C. Santiago, and J.A. Izatt, "Detailed visualization of the anterior segment using Fourier-domain optical coherence tomography," Arch. Ophthalmol. **126**, 765–771 (2008).

#110266 - $15.00 USD Received 17 Apr 2009; revised 27 May 2009; accepted 2 Jun 2009; published 22 Jun 2009

6. J. Strasswimmer, M.C. Pierce, B.H. Park, V. Neel, and J.F. de Boer, "Polarization-sensitive optical coherence tomography of invasive basal cell carcinoma," J. Biomed. Opt. **9**, 292–298 (2004).
7. A.F. Fercher, C.K. Hitzenberger, G. Kamp, and S.Y. El-Zaiat, "Measurement of intraocular distances by backscattering spectral interferometry," Opt. Commun. **117**, 43–48 (1995).
8. J.F. de Boer, B. Cense, B.H. Park, M.C. Pierce, G.J. Tearney, and B.E. Bouma, "Improved signal-to-noise ratio in spectral-domain compared with time-domain optical coherence tomography," Opt. Lett. **28**, 2067–2069 (2003).
9. R. Leitgeb, C.K. Hitzenberger, and A.F. Fercher, "Performance of Fourier domain vs. time domain optical coherence tomography," Opt. Express **11**, 889–894 (2003).
10. A.F. Zuluaga and R. Richards-Kortum, "Spatially resolved spectral interferometry for determination of subsurface structure," Opt. Lett. **24**, 519–521 (1999).
11. B. Grajciar, M. Pircher, A.F. Fercher, and R.A. Leitgeb, "Parallel Fourier domain optical coherence tomography for in vivo measurement of the human eye," Opt. Express **13**, 1131–1137 (2005).
12. Y. Watanabe, K. Yamada, and M. Sato, "Three-dimensional imaging by ultrahigh-speed axial-lateral parallel time domain optical coherence tomography," Opt. Express **14**, 5201–5209 (2006).
13. Y. Nakamura, S. Makita, M. Yamanari, M. Itoh, T. Yatagai, and Y. Yasuno, "High-speed three-dimensional human retinal imaging by line-field spectral domain optical coherence tomography," Opt. Express **15**, 7103–7116 (2007).
14. M. Wojtkowski, A. Kowalczyk, R. Leitgeb, and A.F. Fercher, "Full range complex spectral optical coherence tomography technique in eye imaging," Opt. Lett. **27**, 1415–1417 (2002).
15. E. Götzinger, M. Pircher, R.A. Leitgeb, and C.K. Hitzenberger, "High speed full range complex spectral domain optical coherence tomography," Opt. Express **13**, 583–594 (2005).
16. M.V. Sarunic, B.E. Applegate, and J.A. Izatt, "Real-time quadrature projection complex conjugate resolved Fourier domain optical coherence tomography," Opt. Lett. **31**, 2426–2428 (2006).
17. A.H. Bachmann, R.A. Leitgeb, and T. Lasser, "Heterodyne Fourier domain optical coherence tomography for full range probing with high axial resolution," Opt. Express **14**, 1487–1496 (2006).
18. Y. Yasuno, S. Makita, T. Endo, G. Aoki, M. Itoh, and T. Yatagai, "Simultaneous B-M-mode scanning method for real-time full-range Fourier domain optical coherence tomography," Appl. Opt. **45**, 1861–1865 (2006).
19. B. Baumann, M. Pircher, E. Götzinger, and C.K. Hitzenberger, "Full range complex spectral domain optical coherence tomography without additional phase shifters," Opt. Express **15**, 13375–13387 (2007).
20. B. Hofer, B. Povazay, B. Hermann, A. Unterhuber, G. Matz, and W. Drexler, "Dispersion encoded full range frequency domain optical coherence tomography," Opt. Express **17**, 7–24 (2009).
21. B. Hofer, B. Povazay, B. Hermann, A. Unterhuber, G. Matz, and W. Drexler, "Dispersion encoded full range frequency domain OCT," Proc. SPIE **7168**, 7168 (2009).
22. A.F. Fercher, W. Drexler, C.K. Hitzenberger, and T. Lasser, "Optical coherence tomography - principles and applications," Rep. Prog. Phys. **66**, 239–303 (2003).
23. B.J. Davis, T.S. Ralston, D.L. Marks, S.A. Boppart, and P.S. Carney, "Autocorrelation artifacts in optical coherence tomography and interferometric synthetic aperture microscopy," Opt. Lett. **32**, 1441–1443 (2007).
24. M. Wojtkowski, V.J. Srinivasan, T.H. Ko, J.G. Fujimoto, A. Kowalczyk, and J.S. Duker, "Ultrahigh-resolution, high-speed, Fourier domain optical coherence tomography and methods for dispersion compensation," Opt. Express **12**, 2404–2422 (2004).
25. B. Cense, N.A. Nassif, T. Chen, M. Pierce, S.H. Yun, B.H, Park, B.E. Bouma, G.J. Tearney, and J.F. de Boer, "Ultrahigh-resolution high-speed retinal imaging using spectral-domain optical coherence tomography," Opt. Express **12**, 2435–2447 (2004).
26. Y. Yasuno, Y. Hong, S. Makita, M. Yamanari, M. Akiba, M. Miura, and T. Yatagai, "In vivo high-contrast imaging of deep posterior eye by 1-μm swept source optical coherence tomography and scattering optical coherence angiography," Opt. Express **15**, 6121–6139 (2007).
27. C. Dorrer, "Influence of the calibration of the detector in spectral interferometry," J. Opt. Soc. Am. B **16**, 1160–1168 (1999).
28. C. Dorrer, N. Belabas, J.P. Likforman, and M. Joffre, "Spectral resolution and sampling issues in Fourier-transform spectral interferometry," J. Opt. Soc. Am. B **17**, 1795–1802 (2000).
29. M. Takeda, H. Ina, and S. Kobayashi, "Fourier-transform method of fringe-pattern analysis for computer-based topography and interferometry," J. Opt. Soc. Am. **72**, 156 (1982).
30. M. Mujat, B.H. Park, B. Cense, T.C. Chen, and J.F. de Boer, "Autocalibration of spectral-domain optical coherence tomography spectrometers for *i*n vivo quantitative retinal nerve fiber layer birefringence determination,", J. Biomed. Opt. **12**, 041205 (2007).
31. M. Lazebnik, D.L. Marks, K. Potgieter, R. Gillette, and S.A. Boppart, "Functional optical coherence tomography for detecting neural activity through scattering changes," Opt. Lett. **28**, 1218–1220 (2003).
32. T. Akkin, C. Joo, and J.F. de Boer, "Depth-Resolved Measurement of Transient Structural Changes during Action Potential Propagation," Biophys. J. **93**, 1347–1353 (2007).

#110266 - $15.00 USD Received 17 Apr 2009; revised 27 May 2009; accepted 2 Jun 2009; published 22 Jun 2009

1. Introduction

Optical coherence tomography (OCT) is a powerful tool for noninvasive imaging of tissue [1], with a resolution that is superior to medical imaging tools such as magnetic resonance imaging or ultrasound. In recent years, OCT has been shown to be especially useful in ophthalmology [2, 3], being capable of high-resolution *in vivo* retinal imaging at video rate [4], as well as imaging the cornea and anterior chamber of the eye *in vivo* [5]. Furthermore, significant progress has been made in the early detection of cancer using OCT, where especially polarization-sensitive OCT provides high-contrast images of developing superficial tumors [6].

The speed with which a complete image can be acquired is a critical parameter in medical imaging. As resolution increases, the need for rapid image acquisition becomes more important, since any movement on the order of the resolution causes motion artifacts in the recorded image. To be able to perform diagnostic measurements on living patients, the imaging speed should therefore be as high as possible to obtain the highest quality images. The development of Fourier-domain OCT (FD-OCT) provided a breakthrough in this respect, as it enables the measurement of a depth scan (A-scan) in a single shot [7]. By using spectrometers equipped with high-speed line-scan cameras, the acquisition speed can be increased significantly. Furthermore, FD-OCT provides a large improvement in signal-to-noise ratio compared to time-domain OCT [8, 9].

The imaging speed can be improved even further through parallel acquisition of multiple A-scans, using a two-dimensional imaging spectrometer [10, 11, 12, 13]. When equipped with an area CCD camera instead of a line-scan camera, an array of transversely separated points on the sample can be imaged onto the CCD in parallel, allowing spectrograms to be recorded for all these points simultaneously. In this case, the time resolution is given by the integration time of the spectrometer CCD camera, which is typically well below 1 ms. Such a 2D-OCT system practically eliminates motion artifacts, while still maintaining a relatively long integration time for each A-scan as compared to scanning FD-OCT.

A downside of FD-OCT is the appearance of mirror images in the final picture. This is due to the complex conjugate term that remains after Fourier transformation of the recorded spectral interferogram, giving rise to a Fourier-domain picture that is always symmetric around zero. The standard solution to remove these mirror images is to set the reference arm length such that all the relevant signal appears at one side of depth $z = 0$. A disadvantage of this approach is that it reduces the useful depth range by a factor of two. In addition, due to the discrete sampling by the pixel-based spectrometer, the low-frequency components (i.e. at depths close to $z = 0$) are detected with highest sensitivity. An OCT system that is capable of removing this mirror image artifact would therefore gain both in depth range [14] and in detection sensitivity [9]. Such 'full-range' OCT has been demonstrated using various techniques that require the recording of multiple phase-coherent A-scans for each transverse position [14, 15, 16, 17], or alternatively employ a phase-shifting mechanism to obtain complex-conjugate-resolved data [18, 19]. This increases system complexity, acquisition time and data size. Very recently, Hofer et al. demonstrated a dispersion-based approach to full-range FD-OCT using an elaborate iterative calculation scheme [20].

In this paper we present blue– for the first time to our knowledge – an OCT system that records two-dimensional, full-range OCT images in a single-shot. We demonstrate that, by using a standard numerical dispersion compensation routine in the limit of large dispersion, any FD-OCT system can be transformed into a real-time full-range OCT system with over 40 dB complex conjugate suppression.

We demonstrate measurements on human skin *in vivo*, as well as on the anterior chamber of a mouse eye *in vitro*. In both cases, we record 1392×1040 pixel images in 0.2 ms integration time. We exploit a dispersion imbalance between the reference and sample arms of our OCT

#110266 - $15.00 USD Received 17 Apr 2009; revised 27 May 2009; accepted 2 Jun 2009; published 22 Jun 2009

interferometer to distinguish between the real signal and the mirror image artifact, and use standard numerical dispersion compensation techniques combined with a peak-finding algorithm to suppress the mirror image artifact by more than 40 dB. Another approach to full-range OCT based on dispersion-encoding has recently been demonstrated by Hofer et al. [20]. While the physical principles of our technique are quite similar to this approach, our method has the significant advantage that it employs a direct, non-iterative image reconstruction scheme. As a result, our post-processing is only slightly slower than a standard FD-OCT system, whereas the approach described in [20] typically requires 2-3 orders of magnitude more computation time. An accelerated version of the algorithm by Hofer et al. [21] does provide good image quality after 80 seconds post-processing time. Currently, our post-processing requires only 4 seconds, leading to a near-real-time full-range OCT system. Further speed improvements are readily possible, enabling real-time full-range OCT at video rates. Although the amount of added dispersion has to be known in advance, we show that this dispersion imbalance is automatically obtained with high accuracy from a standard spectrometer calibration procedure. In contrast to other full-range OCT implementations, our technique is compatible with 2D-OCT. Furthermore, as our method does not become more critical when the spectral bandwidth increases, it can be directly implemented on ultrahigh-resolution OCT systems by simply adding dispersive material in the reference arm.

2. Single-shot full-range OCT using dispersion imbalance

In FD-OCT, a spectral interferogram is recorded between a reference field E_r and a field E_s scattered at a depth z inside the sample. This interferogram is usually expressed as [22]:

$$I(\omega) = |E_r|^2 + |E_s|^2 + 2|E_r E_s| \cos(\omega z/c + \varphi_d(\omega)). \tag{1}$$

Here, c is the speed of light, and $\varphi_d(\omega)$ is a frequency-dependent phase term resulting from dispersion between the reference and sample arms. As dispersion causes a frequency-dependent group velocity in a medium, any dispersion imbalance between the interferometer arms will lead to a frequency-dependent optical path length difference between the interferometer arms. As a result, Fourier-transformation of the interferogram in Eq. (1) gives rise to a broad distribution of path lengths instead of a single sharp peak at depth z. However, note that Eq. (1) can be rewritten as:

$$I(\omega) = |E_r|^2 + |E_s|^2 + E_r^* E_s e^{i\omega z/c + i\varphi_d(\omega)} + E_r E_s^* e^{-i\omega z/c - i\varphi_d(\omega)}. \tag{2}$$

After Fourier transformation, the third and fourth term on the right hand side of Eq. (2) give rise to the peaks at the position of the signal and the mirror image artifact, respectively. These peaks will have a Fourier-transform-limited width only when $\varphi_d(\omega) = 0$, which corresponds to no dispersion imbalance between the interferometer arms.

From Eq. (2) it can be seen that the signal and the mirror image artifact differ in one important aspect, namely the sign of $\varphi_d(\omega)$. When $\varphi_d(\omega)$ is known (e.g. through calibration), one can compensate the dispersion numerically by multiplying Eq. (2) with a phase term $\exp(-i\varphi_d(\omega))$, resulting in:

$$I(\omega) = E_r^* E_s e^{i\omega z/c} + E_r E_s^* e^{-i\omega z/c - 2i\varphi_d(\omega)}. \tag{3}$$

Note that the reference autocorrelation term $|E_r|^2$ has been filtered out numerically before applying the dispersion correction, which is achieved by Fourier transformation, removal of the DC component in Fourier space, and inverse Fourier transformation back to the spectral domain. Furthermore, $|E_s|^2$ is neglected since $E_s \ll E_r$. After this numerical dispersion compensation step, the signal peak will be free of phase errors, while the mirror image artifact will have broadened by an additional factor of two. By implementing a large dispersion imbalance (by

#110266 - $15.00 USD Received 17 Apr 2009; revised 27 May 2009; accepted 2 Jun 2009; published 22 Jun 2009

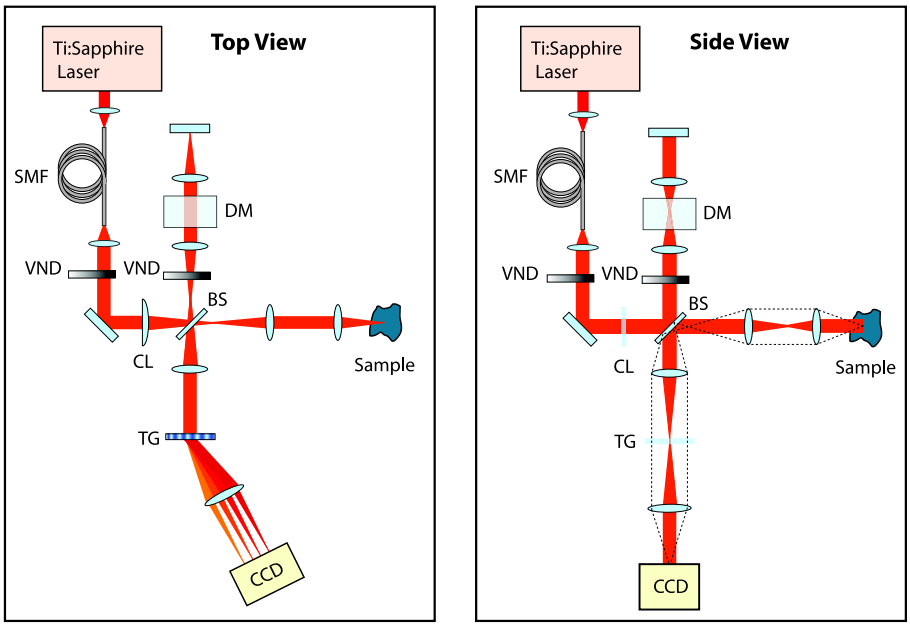

Fig. 1. Schematic drawing of the single-shot 2D-OCT system. In the top view, the beam is focused on the sample, and a spectral interferogram is recorded from the scattered light at this position. In the side view, a collimated beam illuminates the sample, and the sample is imaged onto the CCD camera. The dashed lines indicate the imaging rays. SMF: single-mode fiber, VND: variable neutral-density filter, CL: cylindrical lens, BS: 50/50 beamsplitter, DM: dispersive material, TG: transmission grating, CCD: 1392×1040 pixel CCD camera.

placing a large amount of glass in one interferometer arm), a strong suppression of the mirror image artifact can be achieved. A spatial analog of this effect has recently been observed in interferometric synthetic aperture microscopy (ISAM) [23]. Here, the autocorrelation artifacts are defocused instead of refocused upon numerical ISAM reconstruction, since they have a different spatial phase distribution compared to the true scattered signal.

An important advantage of our approach for full-range OCT is that only one A-scan needs to be recorded, where other techniques require up to five A-scans [14] with precisely controlled relative phases. As it does not rely on moving parts or precisely controlled imaging conditions, it can easily be implemented in parallel 2D-OCT. Furthermore, it can be implemented in ultrahigh-resolution FD-OCT systems [24, 25] with minimal additional effort, in contrast to many other full-range OCT techniques.

3. Experimental techniques

3.1. Single-shot full-range 2D-OCT system

The light source of our OCT system is a modelocked Ti:Sapphire laser, producing 140 fs pulses at 808 nm. To shorten the coherence length, the laser pulses are spectrally broadened by self-phase-modulation in a single-mode fiber. At the fiber output, the pulses have a near-Gaussian spectrum with a full-width at half-maximum (FWHM) of 60 nm, and a Gaussian transverse beam profile. A schematic overview of the single-shot 2D-OCT system is given in Fig. 1. After the fiber, a line focus is created using a cylindrical lens. This line focus is relay-imaged onto the sample and the reference mirror using pairs of achromatic doublet lenses. After the inter-

#110266 - $15.00 USD Received 17 Apr 2009; revised 27 May 2009; accepted 2 Jun 2009; published 22 Jun 2009

ferometer, a holographic transmission grating (600 lines/mm) is placed in the Fourier plane of the imaging system. As the grating only disperses in one dimension, the setup behind the interferometer works as a spectrometer in one dimension (the top view in Fig. 1), and simply as an image relay in the other dimension (the side view). In this way, points from different parts on the line focus are imaged above each other on the spectrometer CCD camera, and a full spectral interferogram is recorded for all points simultaneously. The CCD camera (Lumenera Infinity 3-1M) contains 1392×1040 pixels, so 1040 A-scans are recorded in parallel for each camera exposure.

The $f = 10$ cm cylindrical lens creates a 6 μm wide line focus with a transverse width of 6 mm (FWHM), ensuring that the entire height of the CCD camera is used. Since the imaging system from the sample to the camera has a magnification of unity, the transverse resolution is determined by the camera pixel size of 6.45 μm. The 1040 pixels wide CCD chip ensures a transverse imaging range of 6.7 mm. The spectrometer has been set up to measure a 66.3 THz wide frequency range centered at a wavelength of 808 nm, corresponding to an axial pixel step size of 2.2 μm. This frequency range leads to a spectral resolution of 47 GHz per pixel for our 1392-pixel spectrometer. The Fourier transform of the broadened laser spectrum provides an axial resolution of 5 μm, with an axial measurement range that runs from $z = -1.6$ mm to $z = +1.6$ mm. The recorded spectra were not zero-padded. Before Fourier transformation, the spectra are resampled onto a linear frequency scale through cubic spline interpolation. Details of the nonlinear mapping function that is used in this resampling are given in Sec. 3.5.

In comparison to scanning FD-OCT systems, a clear advantage of our 2D-OCT setup is the superior image acquisition speed, as a full 1392×1040-pixel image is recorded in only 0.2 ms (see Sec. 4), practically eliminating motion artifacts. Furthermore, recording all A-scans simultaneously is highly desirable in nonstationary samples. A downside of 2D-OCT compared to scanning FD-OCT are the stringent requirements on the imaging system and the possibility of coherent crosstalk between adjacent pixels [11]. While crosstalk does not limit the resolution in the present system, the degradation of the system sensitivity versus depth does seem to be stronger compared to scanning FD-OCT systems. This can be attributed to the limited Rayleigh range of the imaging optics, which is around 1 mm in the current system. Since a 2D-OCT system inherently couples the imaging conditions for spatial and spectral imaging, this limited depth-of-field also affects the sensitivity at high depths, which is usually not the case in fiber-based scanning FD-OCT systems. However, it should be stressed that these issues can be alleviated by designing the system with a longer Rayleigh range.

The intensity in the line focus at the sample position is 9 mW in all measurements presented here, which equals an average power of 8.7 μW per A-scan. As conventional FD-OCT systems typically use ~ 1 mW in a focal spot of ~ 10 μm diameter, the power per unit area is about two orders of magnitude lower in our system. This is due to the higher integration time per pixel in our 2D-OCT system, where the entire line is illuminated continuously, while in conventional FD-OCT the dwell time of the focused laser spot per pixel is limited.

3.2. Numerical dispersion compensation

To characterize the dispersion compensation in our OCT system, the signal of a plane mirror is measured with varying amounts of dispersive material in the reference arm of the interferometer. The effect of dispersion on the width of the signal is shown in Fig. 2(a), where no numerical dispersion compensation is performed. The effect of increasing dispersion on the width of the peaks is clearly seen. Numerical dispersion compensation by phase correction, which is achieved by multiplication of the data in frequency space by a phase function $\exp(-i\varphi_d(\omega))$, results in a signal of the form given by Eq. (3), as displayed in Fig. 2(b). This procedure retrieves a signal peak with an axial width limited by the light source bandwidth. The mirror

#110266 - $15.00 USD Received 17 Apr 2009; revised 27 May 2009; accepted 2 Jun 2009; published 22 Jun 2009

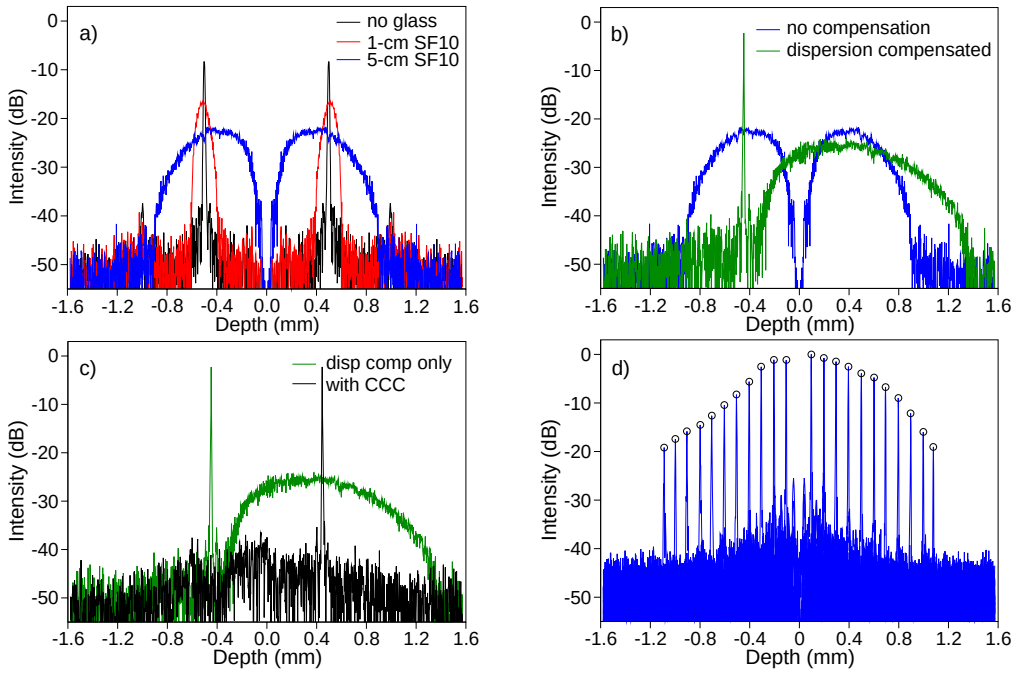

Fig. 2. Fourier transforms of measured spectral interferograms with a mirror as the sample object. a) The effect of dispersion on the OCT signal from a single scatterer. The addition of increasing amounts of dispersive material in one interferometer arm induces a pronounced broadening of both the observed signal and its complex conjugate. b) Numerical dispersion compensation retrieves a signal peak of Fourier-limited width, while the complex conjugate broadens by an additional factor of two. c) Demonstration of the complex-conjugate cancellation (CCC) algorithm. The narrow compensated signal peak is detected and set to zero. Subsequently, the phase of the complex conjugate peak is numerically compensated, leading to a single narrow peak without mirror image. d) System sensitivity as a function of depth. The slight asymmetry is due to the system alignment, while the decrease at higher depths is due to the discrete nature of our pixel-based spectrometer and the finite Rayleigh range of our imaging system.

image artifact is seen to broaden by an additional factor of two. Note that the broadened mirror image artifact appears asymmetric: in the limit of large group-velocity dispersion, an ultrashort pulse acquires a temporal structure that resembles its spectrum, which is slightly asymmetric in our case.

It is interesting to note that a numerical dispersion compensation routine as described here is used regularly in FD-OCT to compensate for slight degradations in axial resolution [24, 25]. In contrast, here we exploit numerical dispersion compensation in the presence of a large dispersion imbalance, and demonstrate that this approach enables full-range OCT. The only required modification to an existing FD-OCT system is the addition of a significant amount of dispersion to one of the interferometer arms.

The dispersion-based method for full-range OCT presented here is particularly useful in the context of single-shot 2D-OCT (see [10, 11, 12, 13] as well as the setup presented here), for which other full-range OCT techniques based on phase shifting or recording of multiple A-scans are difficult to implement.

#110266 - $15.00 USD Received 17 Apr 2009; revised 27 May 2009; accepted 2 Jun 2009; published 22 Jun 2009

3.3. *The complex-conjugate cancellation algorithm*

While the dispersion compensation scheme discussed in Section 2 already provides a strong suppression of the mirror image artifacts, it has the drawback that the scattered intensity of the mirror image artifacts is still present in the final image, leading to a homogeneous but nonconstant background. An algorithm capable of removing the artifacts completely would further reduce and smoothen the background, leading to an increase in dynamic range.

Such an improvement can be achieved with a fast and conceptually simple technique which we denote as the "complex-conjugate cancellation (CCC) algorithm". The basis of this method is the realization that after dispersion compensation, the signal peak corresponding to an individual scatterer is localized in a few pixels in z-space, while its mirror image is distributed over a large part of the z-axis. By identifying this narrow peak and setting these few z-pixels to zero, the signal peak is effectively removed, leaving only the broad mirror image, of which the phase corresponds to $-2\times\varphi_d$ (see Eq. (3)). The remaining depth image is then Fourier transformed to frequency space, multiplied with a factor $\exp(+2i\varphi_d(\omega))$, and inverse Fourier transformed back to z-space. This results in dispersion compensation for the mirror image, turning this initially broad distribution into a sharp peak. Thanks to the cancellation of the initial sharp peak, this final signal is completely free of mirror image terms, providing a true full-range image. In reality, cancellation of only the most dominant signal peaks already provides a complex-conjugate suppression ratio of over 40 dB. We find that a simple peak finding algorithm, which locates and removes any peak exceeding $\sim 30\%$ of the highest measured peak intensity, is sufficient for our typical samples (see Sec. 4). Therefore, this CCC algorithm requires only a standard peak finding routine, two fast Fourier transformations (FFT's) and a phase multiplication, making it fast and easy to implement. In total, the steps taken for full-range image processing are:

1. Remove DC component from raw data: FFT, removal of $z=0$ peak, and FFT^{-1}.
2. Resampling of the data from pixel-space to frequency-space.
3. Phase multiplication with $\exp(-i\varphi_d(\omega))$.
4. FFT.
5. Peak removal algorithm.
6. FFT^{-1}.
7. Phase multiplication with $\exp(+2i\varphi_d(\omega))$.
8. Final FFT.

Where steps $4-7$ constitute the CCC algorithm, while the other steps are the standard FD-OCT algorithm with numerical dispersion compensation.

The effect of the CCC algorithm is demonstrated in Fig. 2(c). The few-pixel-wide dispersion-compensated signal peak is set to zero, after which the phase compensation is performed for the complex conjugate peak. This results in a sharp peak at the position of the complex conjugate, while the dispersion-broadened background has disappeared completely.

Figure 2(d) shows a measurement of the decrease in system sensitivity as a function of depth, which is due to the discrete nature of the pixel-based spectrometer, and to the limited Rayleigh range of the imaging system. The measurement dynamic range is found to be 45 dB, while the sensitivity decreases by 10 dB at a depth of 0.8 mm. While in a standard FD-OCT system only half this depth range can be used (on one side of $z=0$), our full-range OCT system can record signals at both sides of $z=0$ simultaneously, effectively doubling the axial measurement range.

#110266 - $15.00 USD Received 17 Apr 2009; revised 27 May 2009; accepted 2 Jun 2009; published 22 Jun 2009

As an added benefit, full-range OCT also enables a more effective use of the depth range around $z = 0$, where the detection sensitivity is highest.

The exact amount of dispersion imbalance is not critical for proper operation of the CCC algorithm. We find that a dispersive broadening of the mirror image by a factor $\sim 10^2$ provides highly robust operation. Stronger broadening will of course lead to a higher reduction through the numerical dispersion compensation step, but is not required for the CCC algorithm, as the dominant peaks can already be filtered out effectively at lower broadening. Note that extreme amounts of dispersion can lead to signals that are broadened beyond the depth range of the spectrometer. This situation should be avoided, as it would limit the effective spectral bandwidth over which interference is detected, resulting in a decrease of axial resolution.

The CCC algorithm is intrinsically fast, since it requires only a single-step peak cancellation procedure instead of an iterative routine. The entire processing of a 1392×1040 2D-OCT recording to a full-range image including complex-conjugate cancellation takes only 4 seconds on a standard desktop computer (LabView, Intel 1.86 GHz dual core processor, 2 GB RAM). It should be noted that the most time-consuming processing step is the frequency-axis resampling (step 2), and that the CCC algorithm increases the processing time by only 0.8 seconds. No effort has yet been undertaken to improve the computational efficiency of e.g. fast-Fourier-transforms over the standard LabView implementations. With such further improvements in processing speed, our system can conveniently be used for real-time viewing of full-range 2D-OCT images at video rates.

3.4. Characterization of system parameters

To characterize the system parameters, we performed calibration measurements of both the transverse spatial and the axial resolution. Transverse spatial resolution calibration is performed by imaging a USAF 1951 resolution target (Fig. 3(a)), specifically the lines in Group 5. The highest resolution structures (element 6) in this group has a resolution of 57 line pairs per mm, corresponding to a line width of 8.8 μm. An single-shot 2D-OCT image of the Group 5 pattern is shown in Fig. 3(b), which clearly shows that all the structures in this group are well-resolved. Figure 3(c) displays the intensity along the imaged line. This graph proves that the transverse resolution of our imaging system actually corresponds to the theoretically expected value of 6.45 μm.

From Fig. 3(c) we conclude that coherent crosstalk is not a limiting factor in our imaging system, in contrast to reports by others [11]. This is due to our imaging system, which has been set up to oversample in the transverse spatial dimension, leading to a diffraction limited spot size that is smaller than the CCD pixel size. Oversampling has the advantage that the transverse resolution is limited by the camera pixels, and that crosstalk between adjacent pixels is suppressed. The disadvantage of oversampling is that due to the smaller diffraction limit of the imaging system, the Rayleigh range at the sample position is reduced, leading to an increased reduction of the measurement sensitivity with depth.

Calibration of the depth resolution is performed by imaging a stack of 170 μm thick microscope coverslips (285 μm optical thickness), with some random air spaces between them. After proper image reconstruction, involving all the steps described in Sec. 3.3, all reflections from the coverslip surfaces are observed to have a transform-limited resolution of 5 μm. The image of the coverslips is shown in Fig. 3(d), while Fig. 3(e) shows a single A-scan extracted from Fig. 3d, demonstrating the 5 μm axial resolution. The constant axial resolution as a function of depth is expected at the current source bandwidth, where sample-induced dispersion is not significant yet. When using larger source bandwidths for ultrahigh-resolution OCT, then the dispersion caused by the sample needs to be considered as well [24, 25].

#110266 - $15.00 USD Received 17 Apr 2009; revised 27 May 2009; accepted 2 Jun 2009; published 22 Jun 2009

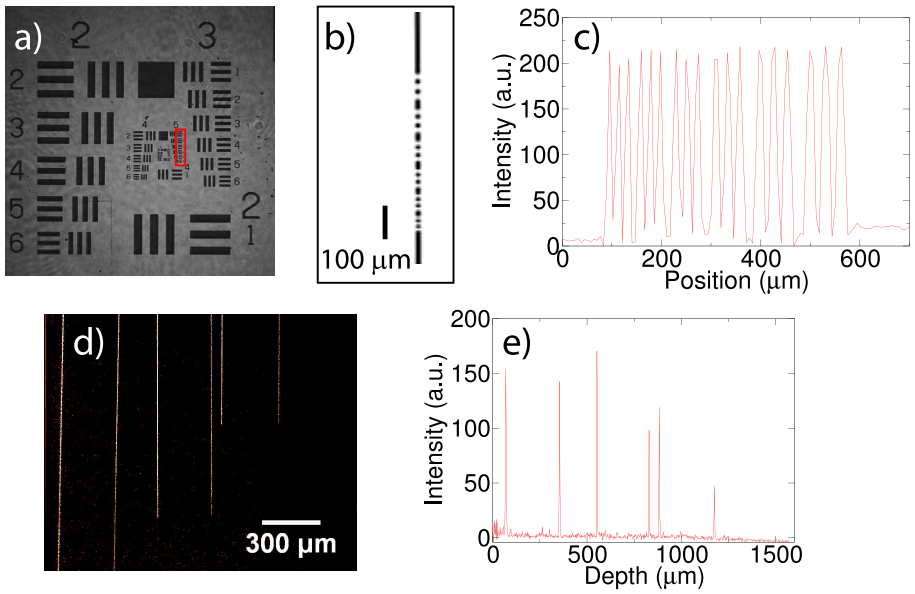

Fig. 3. a) USAF 1951 resolution test target, the elements of Group 5 are highlighted by the red box. b) OCT recording of the Group 5 elements. c) Transverse intensity profile of the Group 5 elements shown in b. The smallest elements are well-resolved. d) Image of a stack of three coverslips with random air space in between, used for axial resolution measurement. e) Single A-scan taken from the coverslip-image. All peaks have a Fourier-transform-limited width of 5 μm.

3.5. Simultaneous calibration of spectrometer and dispersion imbalance

The full-range dispersion compensation algorithm requires an accurate knowledge of the dispersion imbalance between the interferometer arms. Previous studies that incorporated numerical dispersion compensation relied on iterative least-squares estimation techniques using a sharpness metric [20, 26]. Here we show that the dispersion imbalance in the interferometer can directly be measured during the calibration of the spectrometer axis.

Accurate spectrometer calibration is an essential part of FD-OCT, since the FFT algorithm requires data that is equally spaced in frequency space, while a grating-based spectrometer samples data in (almost) constant wavelength intervals. Therefore, a nonlinear resampling of the spectrometer data is required to obtain a proper depth scan after Fourier transformation [27, 28].

Although a rough calibration can be performed by illuminating the spectrometer with a light source of known spectral intensity profile, a much higher accuracy can be achieved by placing a mirror in the sample arm and recording interferograms at multiple z-positions. Extraction of the spectral phase at each z is performed by the algorithm introduced by Takeda et al [29]. First, the interference signal is isolated by Fourier filtering, leading to an interference signal of the general form $I(\omega) = Ae^{i\theta}$. The spectral phase is extracted by taking the imaginary part of the logarithm of this interference signal:

$$\Im[\ln(Ae^{i\theta})] = \Im[\ln A + i\theta] = \theta \tag{4}$$

This spectral phase is numerically unwrapped to remove 2π phase jumps and fitted to a linear function. This linear fit gives the average phase step per pixel at the given depth z. By measuring z to 1 μm precision and repeating this measurement at 100 μm intervals, the frequency interval per pixel is obtained with 10^{-4} accuracy.

#110266 - $15.00 USD Received 17 Apr 2009; revised 27 May 2009; accepted 2 Jun 2009; published 22 Jun 2009

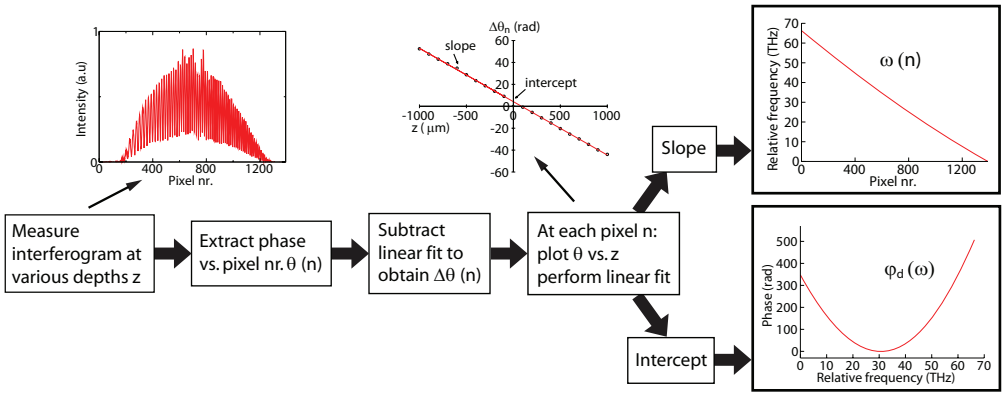

Fig. 4. Flow diagram of the procedure for simultaneous calibration of spectrometer error and dispersion imbalance.

In principle, the argument θ of the complex exponential is given by Eq. (2) as $\theta = \omega z/c + \varphi_d(\omega)$. However, the spectrometer samples in pixel number n rather than in frequency ω. As a result, the measured increase of θ between adjacent spectrometer pixels as a function of z will not be constant. The frequency ω_n at pixel number n can be written as:

$$\omega_n = \Delta\omega_l\, n + \Delta\omega_{nl}(n), \tag{5}$$

which divides the pixel-to-frequency mapping in a linear part with increment $\Delta\omega_l$, and a nonlinear mapping spectrometer function $\Delta\omega_{nl}(n)$. Due to this nonlinear mapping, the actual measured value of θ at pixel n is given by:

$$\theta_n = (\Delta\omega_l\, n + \Delta\omega_{nl}(n))\, z/c + \varphi_d(n). \tag{6}$$

From the linear fit of the measured θ as a function of n (at given z), one obtains the $\Delta\omega_l\, n$ term on the right hand side of Eq. (6). Subtraction of this term then leaves the nonlinear part of the measured phase:

$$\Delta\theta_n = \Delta\omega_{nl}(n) z/c + \varphi_d(n), \tag{7}$$

which shows that the nonlinear spectrometer mapping function $\Delta\omega_{nl}(n)$ introduces an error that is proportional to the depth z, while the dispersion imbalance is modified in a z-independent way. Separation of these terms can thus be achieved by measuring θ_n at different values of z. From a linear fit of $\Delta\theta_n$ versus z at each pixel, the nonlinear spectrometer mapping function $\Delta\omega_{nl}(n)$ is obtained from the slope, while the intercept at $z = 0$ provides the dispersion imbalance $\varphi_d(n)$. The spectrometer mapping function can then be used to obtain the exact dispersion imbalance as a function of frequency $\varphi_d(\omega)$. A flow diagram of the calibration procedure is displayed in Fig. 4. It is worth mentioning that if the dispersion imbalance were negligible (or already be known through other means) measurements at multiple depths would not be required anymore, and a single measurement at one z would suffice to obtain the spectrometer mapping function [30].

As a result, an exact dispersion profile can directly be obtained, and no iterative estimation of the dispersion is needed [20, 26]. It should be noted that in specific cases, where there is a significant amount of material in front of the sample (such as in retinal imaging), then an estimation procedure remains necessary. In the measurements on e.g. skin or the anterior chamber of the eye (as presented in the next Section of this paper), the dispersion calibration procedure performs very well, which is confirmed by the transform-limited peak widths observed in the processed images.

#110266 - $15.00 USD Received 17 Apr 2009; revised 27 May 2009; accepted 2 Jun 2009; published 22 Jun 2009

4. Results and discussion

4.1. Single-shot 2D OCT imaging

We demonstrate the capability of our system by performing measurements on skin tissue of a healthy human volunteer. Figure 5(a) shows an imaged depth section of a fingertip. The recorded images compare well to those taken with standard FD-OCT systems, showing significant structural details such as 70 μm wide sweat ducts.

Aside from *in vivo* measurements on human skin, the 2D-OCT system can be applied for ophthalmic imaging as well. At present, ophthalmology is one of the main applications of OCT, and we tested the capability of our system in this field by imaging the anterior chamber of a mouse eye recorded *in vitro*. A typical image is shown in Fig. 5(b). From the image it is clear that the eye has undergone some post-mortem structural changes, such as an increased lens opacity and a decrease of the aqueous humour. Nevertheless, the various structures in the anterior chamber are clearly visible: cornea, aqueous humour, lens and iris can be distinguished in good detail. In this particular picture, the corneal thickness is measured to be 84 (5) μm. Both images shown in Fig. 5 have been recorded in a single shot of the CCD camera, with an exposure time of 0.2 ms. The intensity scale shown in Fig. 5 is valid for Figs. 6 and 7 as well.

These images were acquired with the sample located on only one side of the $z = 0$ depth. Nevertheless, they were taken with the dispersion imbalance between the interferometer arms present, and the full reconstruction algorithm has been used to obtain these images. The real influence of the dispersion compensation algorithm and full-range OCT is the subject of the next Section.

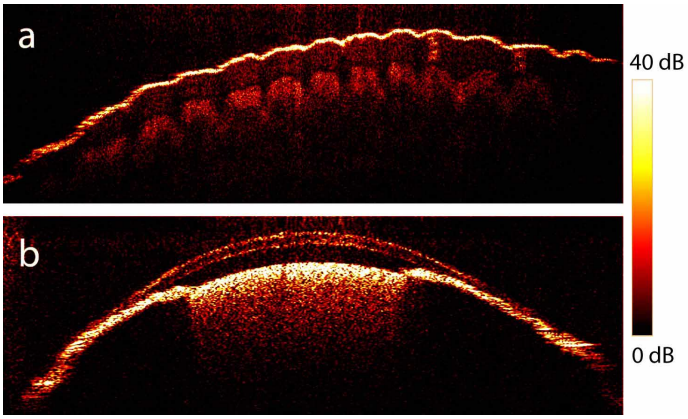

Fig. 5. a) Single-shot 2D-OCT image of a human fingertip in vivo. b) Single-shot 2D-OCT image of a mouse eye anterior chamber in vitro. Both measurements were acquired in 0.2 ms. The image dimensions are 5.8×1.2 mm for a), and 2.7×1.2 mm for b), respectively.

4.2. Dispersion compensation and full-range imaging

For the full-range OCT imaging, we inserted 5 cm of SF10 glass into the reference arm, which produces a group velocity dispersion of 1.87×10^4 fs^2 and a third-order dispersion of 1.21×10^4 fs^3. This amount of dispersion causes features in the depth scan to broaden by a factor of 100. After dispersion compensation, the intensity of the mirror image artifact is reduced by 23 dB. This 23 dB reduction corresponds to the aforementioned factor 100 times two, since the mirror image acquires twice the dispersion phase φ_d after numerical compensation.

#110266 - $15.00 USD Received 17 Apr 2009; revised 27 May 2009; accepted 2 Jun 2009; published 22 Jun 2009

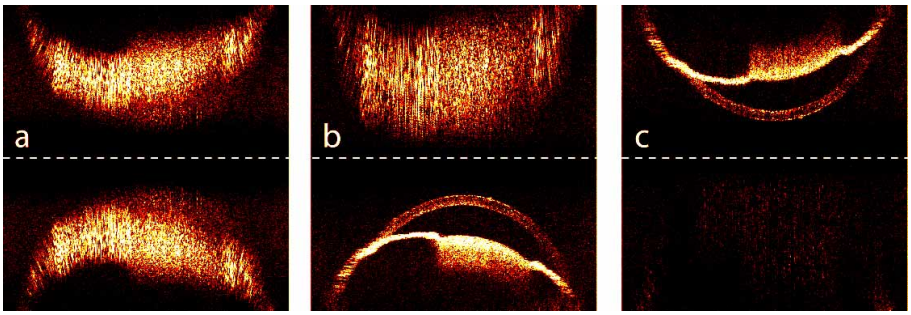

Fig. 6. Demonstration of single-shot full-range 2D-OCT using dispersion compensation. a) Depth image without dispersion compensation. b) Depth image with dispersion compensation. The image appears sharp, while the mirror image is broadened by an additional factor of two. c) Depth image with both dispersion compensation and the CCC algorithm. Over 40 dB suppression of the mirror image is achieved. Image size is 3.0×3.2 mm (w $\times$ h), the dashed line indicates $z = 0$. The intensity scale is identical for all three images.

The effect of the dispersion imbalance on the OCT image is shown in Fig. 6(a), displaying a single-shot recording of the anterior chamber of a mouse eye in vitro without numerical dispersion compensation. The signals smear out over a large depth range, while remaining symmetrical around $z = 0$. Numerically compensating the dispersion by multiplying the resampled interferogram with the calibrated dispersion phase according to Eq. (3) leads to Fig. 6(b). The signal now appears sharp, displaying a 5 μm depth resolution, while the complex conjugate has broadened even more, mostly contributing as a smooth background profile. To further reduce the influence of this complex conjugate background, the CCC algorithm is applied, resulting in the image in Fig. 6(c). The peak-finding algorithm cancels out the sharpest features in Fig. 6(b), and subsequently applies a dispersion compensation step to cancel the dispersion for the complex conjugate signals. This results in an image in which the background due to the mirror image has been suppressed by an additional 20 dB.

To demonstrate true full-range 2D-OCT we shift the $z = 0$ position to a plane inside the sample, leading to an overlap between real image and complex conjugate. The resulting image when using only dispersion compensation is shown in Fig. 7(a). While the image can already clearly be seen, a broad background due to the remaining broadened complex conjugate is still visible, causing a decrease in image contrast. Figure 7(b) shows the image after the additional complex-conjugate cancellation procedure, in which a strong improvement in image contrast is observed, which results from the strongly suppressed complex conjugate background. Note that the aqueous humour has decreased significantly with respect to Fig. 6(c): this is due to slow, continuous degradation of the sample, as the image in Fig. 7 was taken about 30 minutes after the image in Fig. 6.

An interesting observation is that the signal runs continuously across the $z = 0$ line, although the strong DC peak has been explicitly set to zero. This is because of the initial width of the broadened structures before dispersion compensation: the total scattered intensity from a given object is distributed over a significant part of the depth axis. If this distribution happens to be centered close to $z = 0$, then only a few pixels are filtered out together with the DC peak, leaving most of the scattered power present in the image. After dispersion compensation, the sharp peak at $z = 0$ is retrieved. In principle, the removal of some of its spectral components causes the signal peak to broaden by a few percent, but in practice this broadening is much smaller than the spectrometer resolution and is therefore not observed. The possibility of continuous imaging around $z = 0$ is an additional benefit of our dispersion compensation method.

#110266 - $15.00 USD Received 17 Apr 2009; revised 27 May 2009; accepted 2 Jun 2009; published 22 Jun 2009

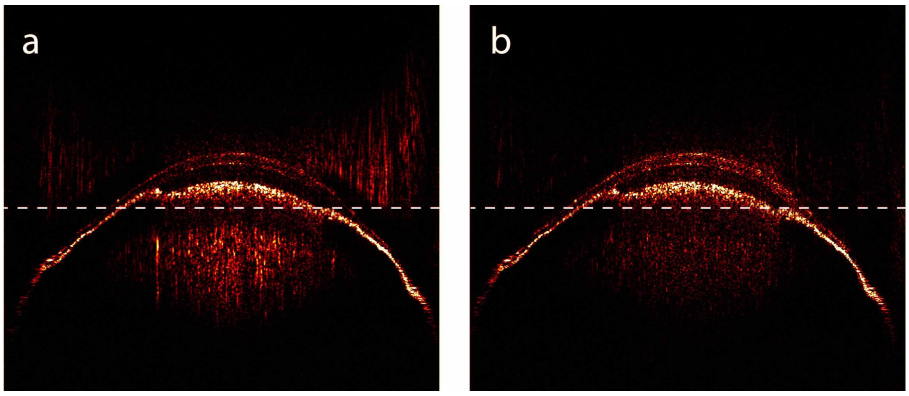

Fig. 7. Single-shot image around zero path length difference ($z = 0$ indicated by the dashed line). a) Image with only dispersion compensation. The mirror-image background is still clearly visible. b) Image with the CCC algorithm. The mirror image background is strongly suppressed, providing a high-contrast full-range image. Image size is 2.8×2.4 mm (w $\times$ h).

5. Conclusions and outlook

The single-shot full-range 2D-OCT system presented here has potential as a fast, robust and flexible diagnostic imaging tool. We envisage various applications in both tissue imaging and ophthalmology. Especially the reduced sensitivity to motion artifacts can make single-shot 2D-OCT a useful improvement compared to conventional FD-OCT.

The single-shot method for full-range OCT through dispersion imbalancing has been demonstrated as an easy and convenient way to increase the measurement range in FD-OCT by a factor of two. It only requires some dispersive material in one interferometer arm, and all the required information on the dispersion is obtained in a standard spectrometer calibration. Therefore, any existing FD-OCT system can be easily upgraded to a full-range device without the need for additional scanning mechanisms. The CCC algorithm has been introduced as a fast, non-iterative procedure, which allows a further reduction of the complex-conjugate artifacts. By combining dispersion compensation and the CCC algorithm, the complex-conjugate artifacts have been suppressed by > 40 dB.

The combination of full-range imaging and 2D-OCT provides a fast imaging tool with a large field of view. State-of-the-art line-scan CCD cameras are capable of recording $140,000$ spectra per second, while swept-source OCT has been demonstrated at $750,000$ A-scans per second. With our current CCD camera running at 30 fps, $31,200$ A-scans can be recorded per second. However, by incorporating state-of-the-art CMOS cameras that run at $7,000$ fps, imaging speeds exceeding 7 million A-scans per second can be achieved. Our current integration time of 0.2 ms would then already be compatible with $5,000$ fps (5 million A-scans) without a loss of signal-to-noise ratio, if a 100% camera duty cycle could be achieved. OCT has been used to detect action potentials in nerve fibers, by detecting changes in scattering intensity [31] and optical path length [32]. While these studies achieved a high time resolution by repeatedly recording an A-scan at one specific location, a 2D-OCT system has the advantage that a full image can be recorded in a single shot. When combined with a faster camera, the system presented here could allow time-resolved 2D-imaging of these important elementary biological processes.

#110266 - $15.00 USD Received 17 Apr 2009; revised 27 May 2009; accepted 2 Jun 2009; published 22 Jun 2009

Acknowledgments

The authors would like to thank Prof. Dr. J.F. de Boer for insightful discussions, and Dr. R.M. Meredith for providing the mouse eye sample.

#110266 - $15.00 USD Received 17 Apr 2009; revised 27 May 2009; accepted 2 Jun 2009; published 22 Jun 2009